Title

EPR Spectroscopic Studies of [FeFe]-Hydrogenase Maturation

Journal

Catalysis Letters, 58(12-13)

ISSN

1011-372X

Authors

Suess, Daniel LM
Britt, R David

Publication Date

2015-09-01

DOI

10.1007/s11244-015-0412-y

Peer reviewed

Published in final edited form as:

Catal Letters. 2015 September ; 58(12): 699–707. doi:10.1007/s11244-015-0412-y.

EPR Spectroscopic Studies of [FeFe]-Hydrogenase Maturation

Daniel L. M. Suess[1] and **R. David Britt**[1]

R. David Britt: rdbritt@ucdavis.edu

[1]Department of Chemistry, University of California, One Shields Avenue, Davis, CA 95616, USA

Abstract

Proton reduction and H_2 oxidation are key elementary reactions for solar fuel production. Hydrogenases interconvert H^+ and H_2 with remarkable efficiency and have therefore received much attention in this context. For [FeFe]-hydrogenases, catalysis occurs at a unique cofactor called the H-cluster. In this article, we discuss ways in which EPR spectroscopy has elucidated aspects of the bioassembly of the H-cluster, with a focus on four case studies: EPR spectroscopic identification of a radical *en route* to the CO and CN^- ligands of the H-cluster, tracing ^{57}Fe from the maturase HydG into the H-cluster, characterization of the auxiliary Fe–S cluster in HydG, and isotopic labeling of the CN^- ligands of HydA for electronic structure studies of its H_{ox} state. Advances in cell-free maturation protocols have enabled several of these mechanistic studies, and understanding H-cluster maturation may in turn provide insights leading to improvements in hydrogenase production for biotechnological applications.

Keywords

Hydrogenase; EPR spectroscopy; Radical SAM enzymes; Fe–S cluster enzymes

1 Introduction

Hydrogenases catalyze the interconversion of H^+ and H_2 and have attracted considerable attention in the context of solar fuel production [1]. The [FeFe]-hydrogenases are highly active [2] and feature a hexa-iron catalytic cofactor known as the H-cluster (Fig. 1), which consists of a [4Fe–4S] subcluster ("$[4Fe–4S]_H$") linked via an L-cysteine ("Cys") residue to a unique di-iron subcluster ("$[2Fe]_H$") [3, 4]. In the last decade, the bioassembly of the H-cluster has emerged as an active topic of research that presents fresh challenges in the coordination chemistry, radical chemistry, and biochemistry of Fe–S enzymes [5]. Unraveling this process is motivated partly by the goal of improving hydrogenase production for biotechnological applications, and partly by its exquisite chemical complexity. The objective of this article is to explicate a few examples in which EPR spectroscopy has provided insight into the mechanism of H-cluster maturation, and to show how the goals of understanding both the mechanism of maturation and the properties of the mature H-cluster are intellectually and practically related. We begin with a brief overview of what is known about H-cluster bioassembly and then focus in greater detail on two

Correspondence to: R. David Britt, rdbritt@ucdavis.edu.

investigations of the maturase, HydG, and two investigations of the mature hydrogenase, HydA. More extensive presentations of other biochemical, spectroscopic, and structural studies can be found in recent reviews [1, 5–10].

A central tenet of HydA maturation is that the H-cluster of HydA is assembled in a stepwise manner: the $[4Fe–4S]_H$ subcluster is generated by the cell's typical Fe-S cluster machinery and the $[2Fe]_H$ subcluster is synthesized and installed by three maturases: HydE, HydF, and HydG (Fig. 1) [11–13]. As such, active HydA is only obtained when it is coexpressed with HydE, HydF, and HydG; when HydA is not coexpressed with the maturases, the resulting H-cluster consists only of the $[4Fe–4S]_H$ subcluster and is called either "$HydA^{\Delta EFG}$" or "apo-HydA." Thus, the primary objective in studying HydA bioassembly is to learn how the maturases synthesize and install the $[2Fe]_H$ subcluster; because Fe–S cluster chemistry is central to these processes, the Fe–S cluster content and function of the maturases will be emphasized herein.

HydE is a member of the radical *S*-adenosyl-L-methionine (SAM) family of enzymes [7] which employs a [4Fe–4S] cluster to coordinate and reduce SAM by one electron to generate the reactive 5′-deoxyadenosyl radical ("5′-dA·"). EPR and UV/visible spectroscopic studies of *Thermatoga maritima* (*Tm*) and *Clostridium acetobutylicum* (*Ca*) HydE suggest that it coordinates both a SAM-binding [4Fe–4S] cluster and an auxiliary [4Fe–4S] cluster [14, 15]. However, not all of the Cys residues implicated in auxiliary cluster binding are strictly conserved, and mutants lacking these residues have been shown to promote HydA maturation (as measured by hydrogenase activity) [16]. Several X-ray crystal structures of *Tm*HydE have been reported, and each shows the presence of a SAM-binding [4Fe–4S] cluster; however, the auxiliary cluster binding site contains only between zero and three Fe atoms, depending on crystallization conditions [16–18]. As such, the relevance of an auxiliary cluster to the function of HydE remains unclear. Moreover, neither the substrate nor the product of HydE has been identified, though it has been recently shown that thiols stimulate SAM cleavage by HydE [15]. Thus, although it has been broadly suggested that HydE may be responsible for synthesizing the 2-azapropane-1,3-dithiolate (ADT) bridging ligand in the $[2Fe]_H$ subcluster [5–7, 9, 15, 19], there is not yet any direct evidence in support of this hypothesis, and HydE's role in H-cluster assembly remains a fertile area for further exploration.

The GTPase, HydF, [20, 21] is also an Fe–S enzyme. The accounts of Fe-S cluster composition of HydF have been considerably variable. When not co-expressed with HydE and HydG, HydF has been reported to show EPR spectroscopic properties consistent with the presence of a [4Fe–4S] cluster [22–25] or of both a [4Fe–4S] cluster and a [2Fe–2S] cluster [20, 26]. When coexpressed with HydE and HydG, HydF displays EPR, FTIR, and XAS spectroscopic features broadly consistent with a $[2Fe]_H$-like subcluster with an additional [4Fe–4S] cluster [20, 27, 28]. It was also shown that HydF (not coexpressed with HydE and HydG) can bind synthetic models of the $[2Fe]_H$ subcluster in a mode that is similar (or identical) to that of the $[2Fe]_H$ subcluster precursor in HydF that is coexpressed with HydE and HydG (and therefore contains the native $[2Fe]_H$ subcluster precursor) [29]. In spite of the considerable progress that has been made toward elucidating the role of HydF

in H-cluster maturation, most of the precise chemical details about the Fe-S cluster conversions that occur on HydF remain up for debate and invite further experimentation.

HydG is a radical SAM enzyme with both a SAM-binding [4Fe–4S] cluster and an auxiliary Fe–S cluster [14, 30–33]. Although the complete reaction promoted by HydG remains unknown, it has been shown that it uses SAM, L-tyrosine ("Tyr"), and Fe to generate an organometallic complex with minimum stoichiometry of $[Fe(CO)_2(CN)]$ that eventually comprises the $[2Fe]_H$ subcluster of HydA [34]. This conclusion was reached primarily by consideration of three sets of experiments which showed: (1) that the CO and CN^- ligands of the $[Fe(CO)_x(CN)_y]$ intermediates observed in HydG are derived from Tyr [34]; (2) that the CO and CN^- ligands of the $[2Fe]_H$ subcluster in HydA are derived from Tyr [35]; and (3) that Fe from HydG is incorporated into the $[2Fe]_H$ subcluster of HydA [34]. These studies built on prior discoveries that HydG produces CN^- [36] and CO [30] from SAM-mediated cleavage of Tyr [37]. Following this brief introduction, we will now further discuss recent insights into the role of HydG in H-cluster maturation obtained from EPR spectroscopy, starting toward the beginning of the HydG reaction: the 5′-dA·-initiated Cα–Cβ of substrate Tyr.

2 Identification of a Radical in the HydG Reaction

It is generally accepted that the HydG reaction is initiated by reductive cleavage of SAM to give the 5′-dA· which abstracts an H atom from substrate Tyr, thereby inducing Tyr Cα–Cβ bond cleavage. Several pathways can be envisioned for this general reaction (Scheme 1), which we will outline here. The first consideration is the site of initial H-atom abstraction. Given that the 5′-dA· abstracts a solvent-exchangeable H-atom [33, 38], the initial site of H-atom abstraction could be either the phenolic H–O atom or the amino H–N atom of Tyr. Many reports and reviews have assumed that the phenolic group is the site of initial H-atom abstraction for both HydG [6, 7, 19, 33, 34, 38, 39] and the closely related Tyr lyase, ThiH [7, 19, 40–42]. The L-tryptophan ("Trp") lyase, NosL, similarly promotes Cα–Cβ cleavage of its substrate amino acid [43], and a recently reported X-ray crystal structure of *Streptomyces actuosus* NosL [44] shows the amino group of substrate Trp oriented toward the 5′-C atom of SAM, suggesting that the amino H–N atom is the likely site of initial H-atom abstraction. On this basis, it was proposed that the amino group of Tyr is, by analogy, the site of initial H-atom abstraction for ThiH and HydG [44]. Although neither of the reported X-ray crystal structures of HydG shows bound Tyr, modeling studies of both structures indicate that Tyr could bind with the amino group oriented toward the site of 5′-dAdo· formation [45, 46], consistent with the proposal based on the NosL structure. Regardless, there are no reports of experimental evidence that distinguishes H–N or H–O atom abstraction for HydG, and therefore both possibilities will be considered here.

Following H–N/O-atom abstraction, the Cα–Cβ bond may be cleaved heterolytically or homolytically (Scheme 1). Homolytic cleavage of the resultant O-centered Tyr radical (**1**) would give *p*-quinone methide (**3**) and a glycyl radical (**4**); the latter would presumably react with further H^+ and e^- equivalents to give the observed *p*-cresol byproduct. Likewise, if the N-centered Tyr radical (**2**) is cleaved heterolytically, the resulting fragments would be *p*-quinone methide (**3**) and, following N-protonation, a glycyl radical (**4**). On the other hand,

heterolytic Cα–Cβ cleavage of the O-centered Tyr radical (**1**) would give the 4-oxidobenzyl radical anion or its protonated form, the 4-hydroxybenzyl radical (collectively referred to herein as the 4(H)OB·, or **5**) as well as dehydroglycine (**6**). Homolytic cleavage of the Cα–Cβ bond of the N-centered Tyr radical (**2**) results in the same two products: the 4(H)OB· (**5**) and dehydroglycine (**6**).

In an attempt to distinguish between these plausible pathways, the discovery and spectroscopic elucidation of radical intermediates were pursued. When the HydG reaction is freeze-quenched early in its time course (<1 min.), an organic radical may be trapped and observed by EPR spectroscopy [33]. Although the hyperfine splitting is poorly resolved in the X-band continuous wave ("CW") EPR spectrum, the Q-band CW EPR spectrum shows a rich hyperfine coupling pattern (Fig. 2, trace A); for this reason, further studies aimed at elucidating the identity of the radical were performed at Q-band [33]. When the radical is generated with $^{2}H_{7}$-^{15}N-Tyr, the corresponding EPR spectrum (Fig. 2, trace B) is dramatically narrower and nearly featureless[1]; this immediately suggests that the radical is Tyr-derived and therefore, unsurprisingly, cannot be the highly reactive 5′-dA· (which has thus far eluded direct spectroscopic observation in any enzyme). The EPR spectrum of the HydG radical generated using ^{13}Cα-Tyr (Fig. 2, trace C) is essentially identical to that generated from natural abundance Tyr; thus, the glycyl radical (**3**)—which is expected to have significant spin density on Cα—can be eliminated as the identity of the observed intermediate. On the other hand, deuteration of only the ring H atoms using 2,3,5,6-$^{2}H_{4}$-Tyr results in a much simpler EPR spectrum (Fig. 2, trace D), which points to significant spin density on the phenol ring of the intermediate. This observation is consistent with the structures of both the O-centered Tyr radical (**1**) and the 4(H)OB· (**5**), and is inconsistent with that of the N-centered Tyr radical (**2**).

Oxygen-centered Tyr radicals such as **1** are well known to have significant spin density on the O atom and alternating ring C atoms (at the 1, 3, and 5 positions) [47, 48]. In contrast, the 4(H)OB· (**5**) is calculated to have significant spin density on the Cβ atom and alternating C atoms in the ring (at the 2, 4, and 6 positions) which would result in substantial spin polariziation of the two Hβ atoms as well as the ring 2- and 6-H atoms [33]. Thus, these two candidate structures may be distinguished by generating the radical using 3,5-$^{2}H_{2}$-Tyr: if the O-centered Tyr radical (**1**) is the correct structure, then the resulting EPR spectrum should be markedly different from that generated using natural abundance Tyr. On the other hand, if the resulting EPR spectrum is little changed from the natural abundance Tyr spectrum, then there must be greater spin density on the 2- and 4-positions than on the 3- and 5-positions, and the 4(H)OB· (**5**) is the correct structure. Because the observed spectrum of the radical generated using 3,5-$^{2}H_{2}$-Tyr (Fig. 2, trace E) is essentially identical to that of the radical derived from natural abundance Tyr (Fig. 2, trace A), it may be deduced that the 4(H)OB· (**5**) is correct. Further support for this assignment came from the EPR spectrum of the radical generated from β,β-^{2}H-Tyr (Fig. 2, trace F), which is dramatically collapsed compared to that of the natural abundance Tyr spectrum and therefore is consistent with a radical that has significant spin density on Cβ.

[1]Radicals with hyperfine coupling to ^{1}H nuclei typically become narrower upon ^{2}H isotopic substitution because of the significantly lower gyromagnetic ratio for ^{2}H.

The observation of the 4(H)OB· (**5**) allows for several mechanistic pathways to be eliminated. In particular, the two pathways invoking the glycyl radical (**3**) may be ruled out in favor of the pathways that invoke the 4(H)OB· (**5**). This finding is particularly relevant to H-cluster maturation because it indirectly suggests that dehydroglycine (**6**) is an intermediate *en route* to the CO and CN^- ligands of the H-cluster.

3 Tracing ^{57}Fe from HydG to HydA Using ENDOR Spectroscopy

The Cα–Cβ bond cleavage of substrate Tyr is only the beginning of the reaction for HydG, which must further cleave dehydroglycine (**6**) to give CO and CN^-. The production of CN^- by HydG was first demonstrated by acidification of the HydG reaction mixture, followed by CN^- derivatization and quantification using fluorescent HPLC analysis [36], and CO production was monitored by in situ addition of deoxymyoglobin which binds free CO to give characteristic UV/visible and IR absorption bands [30]. Subsequent SF-FTIR spectroscopic studies showed the buildup of organometallic $[Fe(CO)_x(CN)_y]$ intermediates, suggesting that the product of the HydG reaction might in fact be an organometallic complex rather than free CO and CN^- [34].

This hypothesis was tested using a previously developed in vitro maturation protocol [35, 49, 50]. First, samples of fully matured and uniformly ^{57}Fe-labeled *Chlamydomonas reinhardtii* (*Cr*) HydA1 ("HydA1^{57Fe}") were generated by coexpression with the *Shewanella oneidensis* (*So*) maturases (HydE, HydF, and HydG) in growth medium that contained ^{57}Fe. In a separate experiment, the maturases were individually expressed, with only HydG grown on ^{57}Fe-containing medium ("HydG^{57Fe}"). Then, natural-abundance apo-HydA1 was matured using HydE, HydF, and HydG^{57Fe} with no additional Fe, and the resulting "HydA1$^{57Fe\text{-}HydG}$" was isolated for EPR spectroscopic analysis in the $S = ½$ H_{ox} state.

The X-band CW EPR spectra of the H_{ox} states of the HydA1^{57Fe} and HydA1$^{57Fe\text{-}HydG}$ samples are broadened in comparison with that of natural-abundance HydA1, indicating some degree of ^{57}Fe incorporation [34]. More detailed information was gleaned from the ^{57}Fe electron-nuclear double resonance ("ENDOR") spectra, which were recorded at $g_1 = 2.10$ where the ENDOR peaks are sharp due to strong orientation selection. The HydA1^{57Fe} ENDOR spectrum displays several features, consistent with ^{57}Fe-labeling of multiple Fe centers in H_{ox} (Fig. 3, trace A). The HydA1$^{57Fe\text{-}HydG}$ ENDOR spectrum is much simpler (Fig. 3, trace B), containing only a doublet with peak positions at $\nu_\pm = ½\cdot A(^{57}Fe) \pm \nu_L$ as expected for a strongly coupled ^{57}Fe nucleus (i.e. $A(^{57}Fe) > 2\cdot\nu_L$) where $A(^{57}Fe)$ and ν_L are the effective hyperfine coupling tensor component and nuclear Larmor frequency, respectively (at a given field position). Thus, the doublet observed in the HydA1$^{57Fe\text{-}HydG}$ spectrum corresponds to $A(^{57}Fe) = 16.0$ MHz and can be ascribed to one of the Fe centers in the $[2Fe]_H$ subcluster (or potentially to both Fe centers if the ^{57}Fe hyperfine coupling is the same for each ^{57}Fe nucleus at this field position). The $A(^{57}Fe) = 16.0$ MHz doublet in the HydA1$^{57Fe\text{-}HydG}$ spectrum cannot correspond to the $[4Fe\text{–}4S]_H$ subcluster because the latter is fully formed in apo-HydA1 and is therefore composed of natural abundance Fe. Consistent with this interpretation is that subtraction of the HydA1$^{57Fe\text{-}HydG}$ spectrum from the HydA1^{57Fe} spectrum yields a clean doublet with $A(^{57}Fe) = 10.55$ MHz

(Fig. 3, trace C) which can be ascribed to the $[4Fe–4S]_H$ cluster. The assignments of the larger and smaller $A(^{57}Fe)$ hyperfine tensors to the $[2Fe]_H$ and $[4Fe–4S]_H$ subclusters, respectively, are in line with previous ENDOR and Mössbauer spectroscopic work on the H_{ox} states of the *Desulfovibrio vulgaris* and *Clostridium pasteurianum* [FeFe]-hydrogenases [51–55], though somewhat different from an ENDOR analysis of H_{ox} from *Desulfovibrio desulfuricans* which suggested $A(^{57}Fe)$ hyperfine tensors of similar magnitude for the two subclusters [56]. Regardless, using ^{57}Fe ENDOR spectroscopy largely as an analytic tool, these studies demonstrate that Fe from HydG is incorporated into the $[2Fe]_H$ subcluster of HydA1.

When viewed in light of the finding that $[Fe(CO)_x(CN)_y]$ intermediates build up in the HydG reaction [34] and that diatomic ligands in these intermediates and in the $[2Fe]_H$ subcluster are derived from Tyr [34, 35], these results suggest that the product of the HydG reaction is an organometallic complex that is eventually incorporated into apo-HydA. The transfer of $[Fe(CO)_x(CN)_y]$ species from HydG to apo-HydA is likely mediated by HydF (though this remains to be directly demonstrated), whereby HydF may serve as an acceptor for the organometallic complex produced by HydG rather than as a [2Fe–2S]-cluster-containing scaffold that is decorated by CO and CN^- ligands produced by HydG [20, 25].

4 Characterization of the Auxiliary Cluster in HydG

Although SF-FTIR spectroscopic studies established that $[Fe(CO)_x(CN)_y]$ intermediates build up in HydG, most of the structural details of these intermediates and the mechanisms by which they are formed and released are still to be determined. EPR spectroscopic evidence for the presence of an auxiliary [4Fe–4S] cluster has been reported for *Tm*HydG [14], *Clostridium acetobutylicum* (*Ca*) HydG [30, 32], and *So*HydG [33]; it has also been suggested that *Ca*HydG may not bind an auxiliary cluster whatsoever [27]. Operating under the assumption that an auxiliary [4Fe–4S] cluster is the site of $[Fe(CO)_x(CN)_y]$ synthon formation, a simple model was proposed in which the non-Cys-ligated Fe of the auxiliary [4Fe–4S] cluster could bind CO and CN^- before the synthon is released to its acceptor [34]. In this manner, the auxiliary cluster could cycle between [4Fe]- and [3Fe]-cluster forms during HydG turnover [34, 57].

An important revision to this mechanism was enabled by an X-ray crystal structure of *Ti*HydG [46], which features two monomers per asymmetric unit: one contains the auxiliary cluster in a [4Fe–4S] form while the other contains an unusual [5Fe–5S] form, consisting of a traditional cuboidal [4Fe–4S] cluster linked to a dangler Fe by a bridging μ_2-sulfide. The dangler Fe (present in 73 % occupancy) is further bound to the protein via a highly conserved His ligand positioned *trans* to the bridging μ_2-sulfide.

The solution EPR spectroscopic features of *So*HydG are consistent with the crystallographically observed 5Fe structure of *Ti*HydG [46]. The X-band CW EPR spectrum of dithionite-reduced *So*HydG shows two major signals with very distinct properties (Fig. 4, panels A and B, top traces). One signal follows typical temperature- and power-dependence for a [4Fe–4S] cluster and has been shown to coordinate SAM [33] (this has also been studied in *Ca*HydG [30, 32]). The other signal is broad and its major resonances occur at

low fields, with g_{eff}-values of 9.5, 4.7, 4.1, and 3.8. The positions of these resonances are indicative of an $S = {}^5/_2$ spin system with a rhombicity of $E/D = 0.255$ as predicted with the aid of a rhombogram [58] or spectral simulation [59]. In general, identification of the spin state of an Fe–S cluster with non-integer spin and $S > ½$ is quite simple using X-band CW EPR spectroscopy because at X-band frequencies, the electron Zeeman term of the spin Hamiltonian is typically much smaller than the zero-field splitting term [58]. Thus, each populated m_S level gives rise to its own EPR signal with g_{eff} values that depend, to a first approximation, only on S and E/D. For the $S = {}^5/_2$ signal in HydG, the resonance at $g_{eff} = 9.5$ arises from the $m_S = \pm ½$ spin manifold, while the resonances at $g_{eff} = 4.7$, 4.1, and 3.8, arise form the $m_S = \pm {}^3/_2$ spin manifold. Because the energy difference between these two manifolds is defined as $2D$ and the relative populations of these spin manifolds are dictated by the Boltzmann distribution, recording and simulating the EPR spectra over a range of temperatures allowed for D to be estimated as +4.5 cm^{-1}.

The $S = {}^5/_2$ spin system observed by EPR spectroscopy may be understood as resulting from exchange coupling between a reduced, $S = ½$ $[4Fe–4S]^+$ cluster and a high-spin $S = 2$ dangler Fe^{2+} center. Nonetheless, it was important to demonstrate that this EPR signal does in fact arise from a [5Fe] cluster with the aforementioned coupling scheme, rather than from a [4Fe–4S] cluster with a highly unusual $S = {}^5/_2$ ground state [60, 61]. To this end, chemical means for removing the dangler Fe to give an $S = ½$ [4Fe–4S] cluster were pursued [46]. Addition of 20 mM KCN to *So*HydG results in partial conversion of the $S = {}^5/_2$ cluster signal to new $S = ½$ signals (Fig. 4, panels A and B, middle traces). When *So*HydG is subjected to three treatments of first diluting with buffer containing KCN, SAM, and sodium dithionite (DTH), and then concentrating through a centrifugal spin concentration filter, nearly quantitative conversion of the $S = {}^5/_2$ signals is achieved (Fig. 4, panels A and B, bottom traces). This process effectively desalts the solution while maintaining constant KCN, SAM, and DTH concentrations, and thereby perturbs the equilibrium set up by KCN addition by driving dangler Fe removal. Further evidence for dangler Fe removal upon addition of exogenous KCN was provided by the ^{13}C hyperfine tensor for $^{13}CN^-$ bound to the [4Fe–4S] cluster species with $g = [2.09, 1.94, 1.93]$. X-band hyperfine sublevel correlation (“HYSCORE”) spectra recorded at multiple field positions were well-simulated using $A(^{13}C) = [-5.0, -4.0, 0.9]$ MHz with Euler angles of [−90°, −40°, 0°] (Fig. 4, panels D and E), parameters that are highly reminiscent of those reported for *Pyrococcus furiousus* ferrodoxin with ^{13}CN bound [62], thereby giving further credence to this structural assignment.

Overall, these structural and spectroscopic studies of the auxiliary cluster of HydG indirectly implicate the dangler Fe as the site of $[Fe(CO)_x(CN)_y]$ synthon formation [46]. Thus, a mechanism involving a [5Fe]↔[4Fe] (or possibly a [5Fe]↔[3Fe]) cluster conversion is likely operative during HydG turnover, the details of which remain to be elucidated. In addition, it is important to note that although a dangler-Fe containing cluster was observed crystallographically for *Ti*HydG and spectroscopically for *So*HydG, no auxiliary cluster whatsoever was observed in the X-ray crystal structure of *Carboxydothermus hydrogenoformans* HydG [45]. Moreover, $S = {}^5/_2$ spin systems have not been reported in the EPR data for *Tm*HydG [14] and *Ca*HydG [30, 32]. The reasons for why dangler Fe-

containing clusters have not been observed in certain HydG studies are not entirely clear. However, given the likely central role of the dangler Fe in both the HydG reaction and in H-cluster maturation, it will be important to resolve any discrepancies regarding the Fe-S cluster composition of HydG.

5 Incorporation of Magnetic Isotopes into the H-Cluster

The final example we've chosen to consider illustrates how protocols developed for H-cluster maturation can be applied toward electronic structure studies of the H-cluster. The H-cluster can be poised in multiple chemical states whose structures and relevance to catalysis are central to understanding the mechanism of H^+/H_2 interconversion [1]. One such state, H_{ox}, has received a great deal of attention because it is thought to be the state from which H_2 is released (for H^+ reduction) or to which H_2 binds (for H_2 oxidation). H_{ox} has an $S = ½$ ground state, with two limiting electronic structure descriptions involving an $S{=}0\,[4\mathrm{Fe}{-}4\mathrm{S}]_{\mathrm{H}}^{2+}$ subcluster exchange-coupled to either a valence-delocalized $S = ½$ $[Fe^{1.5+}Fe^{1.5+}]_H$ subcluster or a valence-localized $S = ½$ $[Fe^{2+}Fe^{1+}]_H$ subcluster. Discriminating between these (as well as other) electronic structure descriptions of H_{ox} requires extensive computational work that is calibrated to the available structural and spectroscopic data [63–65], most commonly the ^{57}Fe hyperfine coupling tensors as determined from ^{57}Fe ENDOR and Mössbauer spectroscopic studies (vide supra) [1, 51–55]. In order to expand the number and variety of hyperfine interactions that can be determined for H_{ox}—and therefore the parameters by which to refine our electronic structure models—a cell-free maturation protocol [35] was employed in order to isotopically label the CN^- ligands of the $[2Fe]_H$ subcluster [66]. In principle, this cell-free maturation technology allows for any atom in the $[2Fe]_H$ subcluster to be labeled with a magnetically active nucleus so long as its small-molecule precursor is known.

The first study toward these ends utilized ^{13}CN- and C^{15}N-labeled H_{ox} samples generated by performing the cell-free maturation with 2-^{13}C-Tyr and ^{15}N-Tyr, respectively [66]; we will focus here on the EPR properties of the ^{13}CN-labeled H_{ox} sample. A strongly coupled ^{13}C hyperfine interaction is readily apparent in the X-band CW EPR spectrum owing to the dramatic splitting of the signal at all three principle g values (Fig. 5). Q-band Davies ENDOR spectra recorded at multiple field positions display features in the "strongly coupled" regime with peaks at $\nu_\pm = ½{\cdot}A(^{13}\mathrm{C}) \pm \nu_L$ (Fig. 5). The high-frequency peaks of these doublets are well separated from other features in the ENDOR spectra, and simulation of their orientation-selected shapes and positions allowed for the hyperfine tensor to be accurately determined ($A(^{13}\mathrm{C})$ = [30.9, 23.2, 30.2] MHz). A more weakly coupled ^{13}C doublet with peaks at $\nu_\pm = \nu_L \pm ½{\cdot}A(^{13}\mathrm{C})$ was observed using the Mims ENDOR pulse sequence, and simulation of the orientation-selected data yielded a hyperfine tensor of $A(^{13}\mathrm{C})$ = [5.22, 5.24, 4.16] MHz. What is most immediately apparent upon comparison of the two ^{13}CN hyperfine tensors is that the magnitudes of their isotropic components ($a_{iso} = ⅓{\bullet}(A_1 + A_2 + A_3)$) are dramatically different—28.1 MHz versus 4.87 MHz—and point to a lopsided spin distribution in H_{ox} wherein the distal Fe (Fe_d) harbors greater spin density than the proximal Fe (Fe_p). This conclusion is in broad agreement with prior computational studies of H_{ox} [63, 65] and in contrast with ^{57}Fe ENDOR studies on H_{ox} in *Desulfovibrio*

desulfuricans, which suggest a more even spin distribution [56]. External ligand binding (e.g. CO, H_2 and/or H_2O) at Fe_d has been invoked as a factor that could give rise to a more even spin distribution [1, 65]; further work aimed at a precise structural-electronic description of H_{ox} is clearly warranted. Nonetheless, this CN^- labeling study illustrates how atom-specific control over H-cluster maturation can enable further refinement of the electronic structure descriptions of catalytically relevant states. A complementary approach, wherein apo-HydA is treated with synthetic $[2Fe]_H$ subcluster precursors to give natural and unnatural variants of holo-HydA, was recently employed for determining the ^{13}C and ^{15}N hyperfine coupling tensors of the CN^- ligands in an unnatural variant of H_{ox} [67]; the observed hyperfine tensors were very similar to those determined for the natural H-cluster generated by the cell-free maturation as described above [66].

6 Conclusion

The examples highlighted in this article illustrate how EPR spectroscopy has played an important role in elucidating several aspects of the mechanism of H-cluster maturation, from the details of Tyr Cα–Cβ bond cleavage to the migration of Fe into the $[2Fe]_H$ cluster of HydA. Advancements in H-cluster maturation protocols have allowed for the execution of otherwise challenging experiments for studying the mature H-cluster, such as incorporating isotopically labeled CN^- into H_{ox}. Conversely, we anticipate that these and future spectroscopic insights into H-cluster maturation may allow for the development of improved maturation protocols with applications for solar fuel production.

Acknowledgments

We gratefully acknowledge funding from the National Institute of General Medical Sciences of the National Institutes of Health (F32GM111025 to D.L.M.S. and GM104543 to R.D.B.).

References

1. Lubitz W, Ogata H, Rüdiger O, Reijerse E. Chem Rev. 2014; 114(8):4081–4148. [PubMed: 24655035]
2. Vincent KA, Parkin A, Armstrong FA. Chem Rev. 2007; 107(10):4366–4413. [PubMed: 17845060]
3. Peters JW, Lanzilotta WN, Lemon BJ, Seefeldt LC. Science. 1998; 282(5395):1853–1858. [PubMed: 9836629]
4. Nicolet Y, Piras C, Legrand P, Hatchikian CE, Fontecilla-Camps JC. Structure. 1999; 7(1):13–23. [PubMed: 10368269]
5. Broderick JB, Byer AS, Duschene KS, Duffus BR, Betz JN, Shepard EM, Peters JW. J Biol Inorg Chem. 2014; 19(6):747–757. [PubMed: 24972661]
6. Shepard EM, Mus F, Betz JN, Byer AS, Duffus BR, Peters JW, Broderick JB. Biochemistry. 2014; 53(25):4090–4104. [PubMed: 24878200]
7. Broderick JB, Duffus BR, Duschene KS, Shepard EM. Chem Rev. 2014; 114(8):4229–4317. [PubMed: 24476342]
8. Duffus BR, Hamilton TL, Shepard EM, Boyd ES, Peters JW, Broderick JB. BBA. 2012; 1824(11): 1254–1263. [PubMed: 22269887]
9. Peters JW, Broderick JB. Annu Rev Biochem. 2012; 81(1):429–450. [PubMed: 22482905]
10. Mulder DW, Shepard EM, Meuser JE, Joshi N, King PW, Posewitz MC, Broderick JB, Peters JW. Structure. 2011; 19(8):1038–1052. [PubMed: 21827941]
11. Posewitz MC, King PW, Smolinski SL, Zhang L, Seibert M, Ghirardi ML. J Biol Chem. 2004; 279(24):25711–25720. [PubMed: 15082711]

12. Mulder DW, Ortillo DO, Gardenghi DJ, Naumov AV, Ruebush SS, Szilagyi RK, Huynh B, Broderick JB, Peters JW. Biochemistry. 2009; 48(26):6240–6248. [PubMed: 19435321]
13. Mulder DW, Boyd ES, Sarma R, Lange RK, Endrizzi JA, Broderick JB, Peters JW. Nature. 2011; 465(7295):248–251. [PubMed: 20418861]
14. Rubach JK, Brazzolotto X, Gaillard J, Fontecave M. FEBS Lett. 2005; 579(22):5055–5060. [PubMed: 16137685]
15. Betz JN, Boswell NW, Fugate CJ, Holliday GL, Akiva E, Scott AG, Babbitt PC, Peters JW, Shepard EM, Broderick JB. Biochemistry. 2015; 54(9):1807–1818. [PubMed: 25654171]
16. Nicolet Y, Rubach JK, Posewitz MC, Amara P, Mathevon C, Atta M, Fontecave M, Fontecilla-Camps JC. J Biol Chem. 2008; 283(27):18861–18872. [PubMed: 18400755]
17. Nicolet Y, Amara P, Mouesca J-M, Fontecilla-Camps JC. Proc Natl Acad Sci USA. 2009; 106(35): 14867–14871. [PubMed: 19706452]
18. Nicolet Y, Rohac R, Martin L, Fontecilla-Camps JC. Proc Natl Acad Sci USA. 2013; 110(18): 7188–7192. [PubMed: 23596207]
19. Swanson KD, Duffus BR, Beard TE, Peters JW, Broderick JB. Eur J Inorg Chem. 2011; 2011(7): 935–947.
20. Shepard EM, McGlynn SE, Bueling AL, Grady-Smith CS, George SJ, Winslow MA, Cramer SP, Peters JW, Broderick JB. Proc Natl Acad Sci USA. 2010; 107(23):10448–10453. [PubMed: 20498089]
21. Vallese F, Berto P, Ruzzene M, Cendron L, Sarno S, De Rosa E, Giacometti GM, Costantini P. J Biol Chem. 2012; 287(43):36544–36555. [PubMed: 22932901]
22. Brazzolotto X, Rubach JK, Gaillard J, Gambarelli S, Atta M, Fontecave M. J Biol Chem. 2006; 281(2):769–774. [PubMed: 16278209]
23. Kuchenreuther JM, Britt RD, Swartz JR. PLoS One. 2012; 7(9):e45850. [PubMed: 23049878]
24. Berggren G, Garcia-Serres R, Brazzolotto X, Clemancey M, Gambarelli S, Atta M, Latour J-M, Hernandez HL, Subramanian S, Johnson MK, Fontecave M. J Biol Inorg Chem. 2013; 19(1):75–84. [PubMed: 24240692]
25. Berto P, Di Valentin M, Cendron L, Vallese F, Albertini M, Salvadori E, Giacometti GM, Carbonera D, Costantini P. BBA. 2012; 1817(12):2149–2157. [PubMed: 22985598]
26. Joshi N, Shepard EM, Byer AS, Swanson KD, Broderick JB, Peters JW. FEBS Lett. 2012; 586(22):3939–3943. [PubMed: 23041346]
27. Czech I, Silakov A, Lubitz W, Happe T. FEBS Lett. 2010; 584(3):638–642. [PubMed: 20018187]
28. Czech I, Stripp S, Sanganas O, Leidel N, Happe T, Haumann M. FEBS Lett. 2011; 585(1):225–230. [PubMed: 21130763]
29. Berggren G, Adamska A, Lambertz C, Simmons TR, Esselborn J, Atta M, Gambarelli S, Mouesca JM, Reijerse E, Lubitz W, Happe T, Artero V, Fontecave M. Nature. 2013; 498(7456):66–69. [PubMed: 23803769]
30. Shepard EM, Duffus BR, George SJ, McGlynn SE, Challand MR, Swanson KD, Roach PL, Cramer SP, Peters JW, Broderick JB. J Am Chem Soc. 2010; 132(27):9247–9249. [PubMed: 20565074]
31. Nicolet Y, Martin L, Tron C, Fontecilla-Camps JC. FEBS Lett. 2010; 584(19):4197–4202. [PubMed: 20837009]
32. Driesener RC, Duffus BR, Shepard EM, Bruzas IR, Duschene KS, Coleman NJR, Marrison APG, Salvadori E, Kay CWM, Peters JW, Broderick JB, Roach PL. Biochemistry. 2013; 52(48):8696–8707. [PubMed: 24206022]
33. Kuchenreuther JM, Myers WK, Stich TA, George SJ, Nejatyjahromy Y, Swartz JR, Britt RD. Science. 2013; 342(6157):472–475. [PubMed: 24159045]
34. Kuchenreuther JM, Myers WK, Suess DLM, Stich TA, Pelmenschikov V, Shiigi S, Cramer SP, Swartz JR, Britt RD, George SJ. Science. 2014; 343(6169):424–427. [PubMed: 24458644]
35. Kuchenreuther JM, George SJ, Grady-Smith CS, Cramer SP, Swartz JR. PLoS One. 2011; 6(5):e20346. [PubMed: 21673792]
36. Driesener RC, Challand MR, McGlynn SE, Shepard EM, Boyd ES, Broderick JB, Peters JW, Roach PL. Angew Chem Int Ed. 2010; 49(9):1687–1690.

37. Pilet E, Nicolet Y, Mathevon C, Douki T, Fontecilla-Camps JC, Fontecave M. FEBS Lett. 2009; 583(3):506–511. [PubMed: 19166853]
38. Duffus BR, Ghose S, Peters JW, Broderick JB. J Am Chem Soc. 2014; 136(38):13086–13089. [PubMed: 25099480]
39. Roach PL. Curr Opin Chem Biol. 2011; 15(2):267–275. [PubMed: 21159543]
40. Challand MR, Martins FT, Roach PL. J Biol Chem. 2010; 285(8):5240–5248. [PubMed: 19923213]
41. Kriek M, Martins F, Challand MR, Croft A, Roach PL. Angew Chem Int Ed. 2007; 46(48):9223–9226.
42. Kriek M, Martins F, Leonardi R, Fairhurst SA, Lowe DJ, Roach PL. J Biol Chem. 2007; 282(24): 17413–17423. [PubMed: 17403671]
43. Zhang Q, Li Y, Chen D, Yu Y, Duan L, Shen B, Liu W. Nat Chem Biol. 2011; 7(3):154–160. [PubMed: 21240261]
44. Nicolet Y, Zeppieri L, Amara P, Fontecilla-Camps JC. Angew Chem Int Ed. 2014; 53(44):11840–11844.
45. Nicolet Y, Pagnier A, Zeppieri L, Martin L, Amara P, Fontecilla-Camps JC. ChemBioChem. 2014; 16(3):397–402. [PubMed: 25504963]
46. Dinis P, Suess DLM, Fox SJ, Harmer JE, Driesener RC, De La Paz L, Swartz JR, Essex JW, Britt RD, Roach PL. Proc Natl Acad Sci USA. 2015; 112(5):1362–1367. [PubMed: 25605932]
47. Hoganson CW, Sahlin M, Sjoberg BM, Babcock GT. J Am Chem Soc. 1996; 118(19):4672–4679.
48. Dole F, Diner BA, Hoganson CW, Babcock GT, Britt RD. J Am Chem Soc. 1997; 119(47):11540–11541.
49. Kuchenreuther JM, Stapleton JA, Swartz JR. PLoS ONE. 2009; 4(10):e7565. [PubMed: 19855833]
50. Kuchenreuther JM, Grady-Smith CS, Bingham AS, George SJ, Cramer SP, Swartz JR. PLoS One. 2010; 5(11):e15491. [PubMed: 21124800]
51. Wang G, Benecky MJ, Huynh BH, Cline JF, Adams M, Mortenson LE, Hoffman BM, Münck E. J Biol Chem. 1984; 259(23):4328–4331.
52. Telser J, Benecky MJ, Adams MW, Mortenson LE, Hoffman BM. J Biol Chem. 1986; 261(29): 13536–13541. [PubMed: 3020036]
53. Telser J, Benecky MJ, Adams MW, Mortenson LE, Hoffman BM. J Biol Chem. 1987; 262(14): 6589–6594. [PubMed: 3032973]
54. Popescu CV, Münck E. J Am Chem Soc. 1999; 121(34):7877–7884.
55. Pereira AS, Tavares P, Moura I, Moura JJG, Huynh BH. J Am Chem Soc. 2001; 123(12):2771–2782. [PubMed: 11456963]
56. Silakov A, Reijerse EJ, Albracht SPJ, Hatchikian EC, Lubitz W. J Am Chem Soc. 2007; 129(37): 11447–11458. [PubMed: 17722921]
57. Pickett CJ. Science. 2014; 343(6169):378–379. [PubMed: 24458630]
58. Hagen, WR. Advances in Inorganic Chemistry. Cammack, R., editor. Vol. 38. Elsevier; New York: 1992. p. 165-222.
59. Stoll S, Schweiger A. J Magn Reson. 2006; 178(1):42–55. [PubMed: 16188474]
60. Onate YA, Vollmer SJ, Switzer RL, Johnson MK. J Biol Chem. 1989; 264(31):18386–18391. [PubMed: 2553706]
61. Boll M, Fuchs G, Tilley G, Armstrong FA, Lowe DJ. Biochemistry. 2000; 39(16):4929–4938. [PubMed: 10769152]
62. Telser J, Smith ET, Adams MWW, Conover RC, Johnson MK, Hoffman BM. J Am Chem Soc. 1995; 117(18):5133–5140.
63. Fiedler AT, Brunold TC. Inorg Chem. 2005; 44(25):9322–9334. [PubMed: 16323916]
64. Greco C, Bruschi M, De Gioia L, Ryde U. Inorg Chem. 2007; 46(15):5911–5921. [PubMed: 17602468]
65. Greco C, Silakov A, Bruschi M, Ryde U, De Gioia L, Lubitz W. Eur J Inorg Chem. 2011; 2011(7): 1043–1049.

66. Myers WK, Stich TA, Suess DLM, Kuchenreuther JM, Swartz JR, Britt RD. J Am Chem Soc. 2014; 136(35):12237–12240. [PubMed: 25133957]

67. Adamska-Venkatesh A, Simmons TR, Siebel JF, Artero V, Fontecave M, Reijerse E, Lubitz W. Phys Chem Chem Phys. 2015; 17(7):5421–5430. [PubMed: 25613229]

68. Pandey AS, Harris TV, Giles LJ, Peters JW, Szilagyi RK. J Am Chem Soc. 2008; 130(13):4533–4540. [PubMed: 18324814]

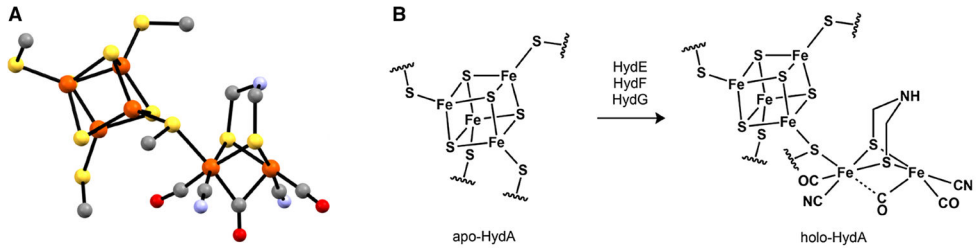

Fig. 1.

a Ball-and-stick representation of the H-cluster from the X-ray crystal structure of *Clostridium pasteurianum* HydA (pdb code 3C8Y [68]) with the dithiolate bridging ligand taken as 2-azapropane-1,3-dithiolate. **b** General scheme of the assembly and installation of the $[2Fe]_H$ subcluster. Color codes: *orange* Fe; *yellow* S; *gray* C; *blue* N; *red* O. The four proteinaceous Cys ligands to the $[4Fe–4S]_H$ subcluster have been truncated

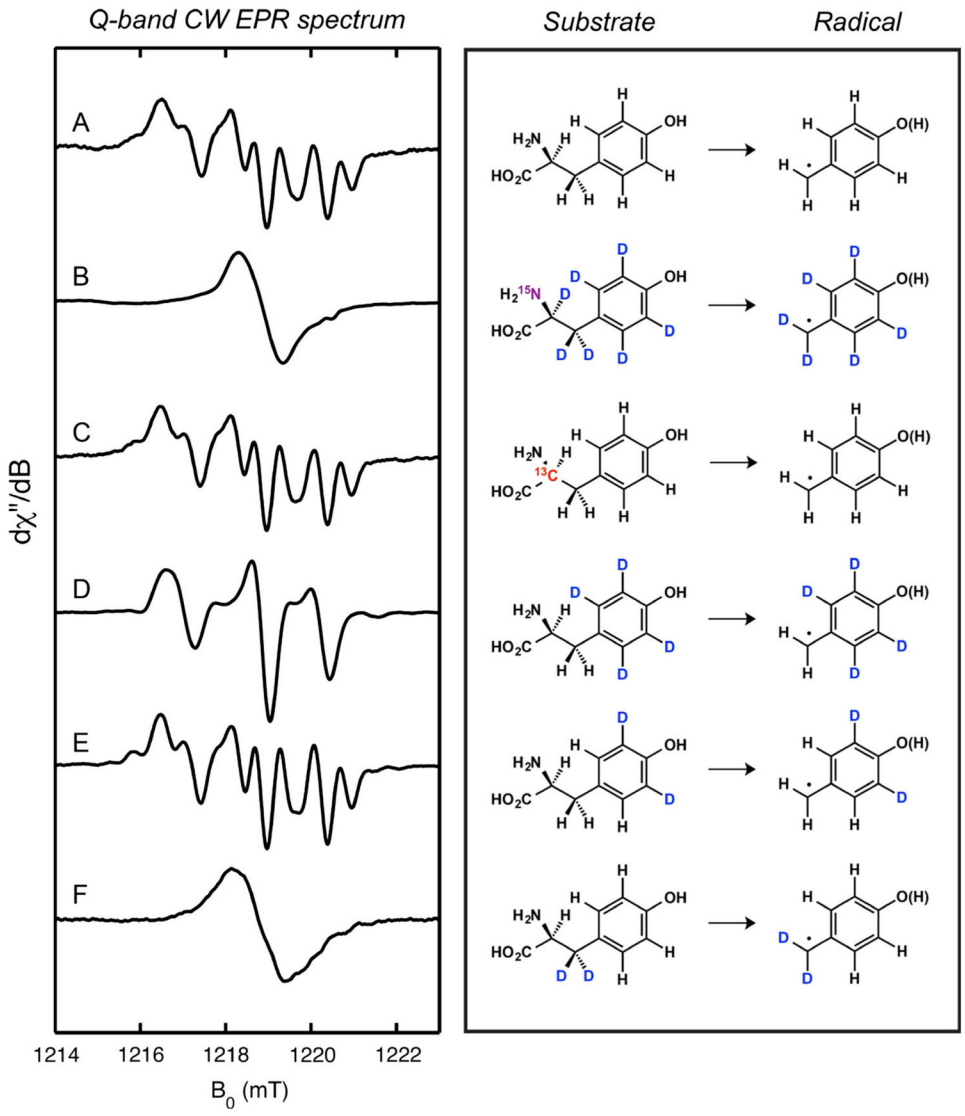

Fig. 2.

Q-band CW EPR spectra of the HydG radical generated with various Tyr isotopologues. Corresponding structural proposals for the radical are shown for clarity. Adapted with permission of the authors from [33]

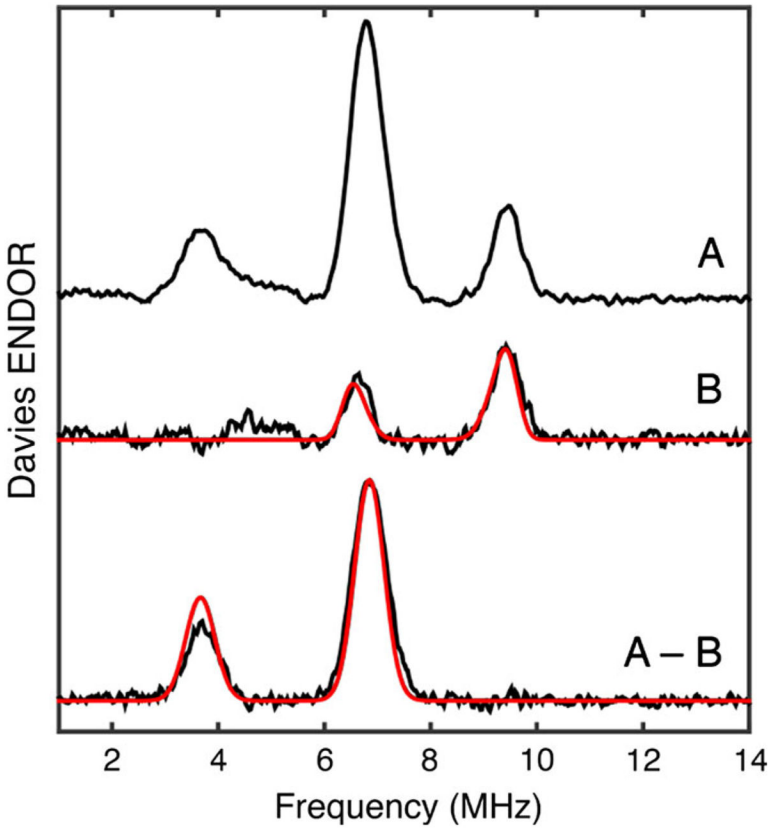

Fig. 3.

Q-band Davies ENDOR spectra of HydA1^{57Fe} (*A*), HydA1$^{57Fe\text{-}HydG}$ (*B*), and the difference spectrum (*A* – *B*), each recorded at g_1 = 2.10. Data (*black*); simulations using hyperfine values from the text (*red*). Adapted with permissions of the authors from [34]

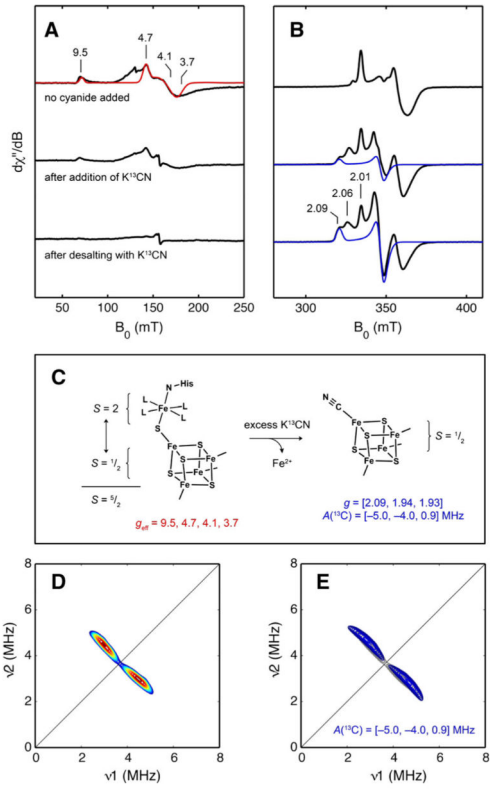

Fig. 4.

EPR studies of the Fe–S cluster composition of dithionite-reduced *So*HydG. **a** and **b** X-band CW EPR spectra recorded at 126 μW (**a**) or 5.00 mW (**b**). *Top traces* spectra of samples with no CN^- added (*black*); simulation of the [5Fe] form of the auxiliary cluster with g_{eff} values indicated (*red*). *Middle traces* spectra of samples with $K^{13}CN$ added (*black*). *Bottom traces* spectra of samples desalted three times in the presence of $K^{13}CN$ as described in the text (*black*) with the g_1 values of the three principle spectral components indicated; simulation of the ^{13}CN-bound [4Fe] form of the auxiliary cluster (*blue*). **c** Simplified exchange coupling scheme for the auxiliary cluster of HydG and the proposed structure of the auxiliary cluster upon treatment with $K^{13}CN$. **d** X-band HYSCORE spectrum recorded at $g = 2.09$ of a sample of *So*HydG desalted three times in the presence of $K^{13}CN$. **e** HYSCORE simulation of the ^{13}CN hyperfine interaction (*blue contours*) with the experimental data from (**d**) reproduced for clarity (*gray contours*). Reproduced with permission of the authors from [46]

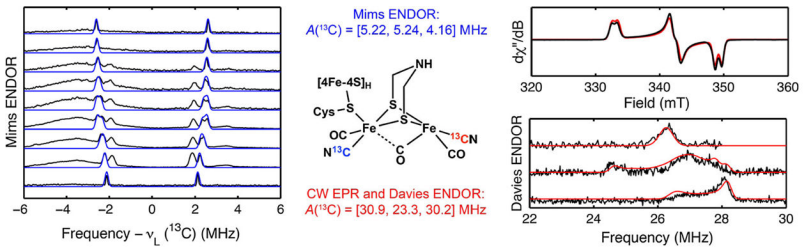

Fig. 5.

EPR studies of ^{13}CN-labeled H_{ox}. Structural assignments and EPR parameters (*center*). Features ascribed to the ^{13}CN ligands bound to the proximal and distal Fe centers are shown in *blue* and *red*, respectively. Orientation-selective Q-band Mims ENDOR data (*black traces, left*) and simulations (*blue traces, left*); the *sharp peaks* that are not simulated here arise from an H_{ox}–CO impurity. X-band CW EPR spectrum (*black trace, right, top*) and simulation (*red trace, right, top*). Orientation-selective Q-band Davies ENDOR data (*black traces, right, bottom*) and simulations (*red traces, right, bottom*). Adapted with permission of the authors from [66]

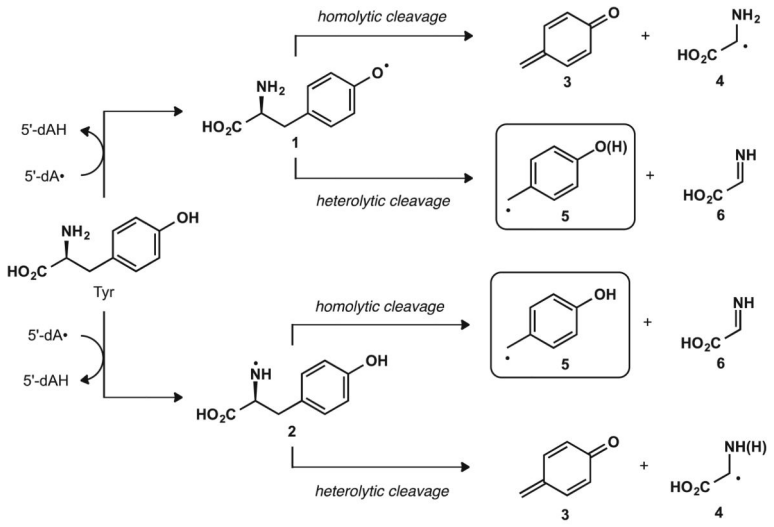

Scheme 1.

Pathways for radical-initiated Tyr Cα–Cβ bond cleavage. Protons denoted in *parentheses* are employed for cases in which the site of H-atom abstraction may undergo subsequent protonation. Only H-atom abstraction from a neutral amine group is shown here; similar pathways may be drawn for H-atom abstraction from an ammonium group